Electrostatically-enriched Lithium Cations Catalyze Biomimetic Aerobic Oxygenation

Shuangshuang Cha[1, †], Yizhou Yang[2, †], Wei Du[1], Tao Jiang[1], Ran Wang[1], Mengxin Qu[1], Zhe Ji[3], Chang Yan[4,5], Xuejing Yang[2, *], Ming Gong[1, *]

[1]Department of Chemistry and Shanghai Key Laboratory of Molecular Catalysis and Innovative Materials, Fudan University, Shanghai, China, 200438

[2]National Engineering Laboratory for Industrial Wastewater Treatment, East China University of Science and Technology, Shanghai, China, 200237

[3]College of Chemistry and Molecular Engineering, Peking University, Beijing 100871, China

[4]Center for Ultrafast Science and Technology, School of Chemistry and Chemical Engineering, Shanghai Jiao Tong University, Shanghai, 200240 China

[5]Zhangjiang Institute for Advanced Study, Shanghai Jiao Tong University, Shanghai, 200240 China

‡ These authors contributed equally.

* Corresponding author. Email: xj.yang@ecust.edu.cn, gongm@fudan.edu.cn

‡ These authors contributed equally.

Abstract

Enzymes often involve short-range electrostatic interactions in the deliberate microenvironment for accelerating the catalysis. Comparatively, electrostatic interactions from ions in solutions are mostly shielded by solvent or counter-ion shells, creating negligible catalytic effects. Herein, we discovered that the Li^+ cations electrostatically accumulated on negatively-charged carboxylated carbon nanotubes could create strong interactions with in-situ formed peroxide anion (OOH^-) intermediates from O_2 reduction, forming an active side-on Li^+-OOH^- complex. This complex reduces the O_2-reduction energy barrier and increases the nucleophilicity, expediting the aerobic oxygenation of ketones. Aside from trapping active intermediates, excessive Li^+ cations also attract the surrounding water dipoles to prevent from quenching the active Li^+-OOH^- complex, highly mimicking the Baeyer Villiger monooxygenase (BVMO). By using probe-assisted quantitative methods, we demonstrated the unique under-coordinative characteristics of interfacial Li^+ with an order of magnitude higher concentration than the bulk solution, providing essential clues about the intrinsic discrepancy between electrocatalytic and thermocatalytic reactivities.

Introduction

Short-range electrostatic interactions are ubiquitous in catalytic systems and play decisive roles in catalytic activity and stereoselectivity[1-4]. The electrostatic attraction between the positively-charged and negatively-charged centers from ions, dipoles or polar functional groups modulates the configurations and energies of the reactants or intermediates, steering toward the targeted reaction pathway[5-8]. These electrostatic interactions are also the selection of nature and drive almost all molecular processes in biological systems, including protein folding, molecular recognition and enzyme catalysis[9-11]. Specifically, the charged centers in enzymes precisely position the key intermediates, toward tremendous rate acceleration and superior selectivity[12,13].

Taking Baeyer Villiger monooxygenase (BVMO) as an example, electrostatic interactions enable the efficient oxygenation of ketones into the corresponding esters using O_2 as the only oxidant, avoiding the use of unstable peracids in conventional processes[14-18]. The catalytic process of BVMO reduces flavin that binds O_2 to form the reactive charged center[17]. Meanwhile, the $NADP^+$ amide establishes a crucial electrostatic interaction with the hydrogen on the flavin's N5 site, which prevents the internal proton transfer to form the undesired hydrogen peroxide. The charged amino residues of the protein scaffold also position the ketone substrate to expedite the nucleophilic attack of the peroxy anion center[19,20]. Inspired by these natural enzymes, researchers have been dedicated to mimicking the enzyme functions, but precisely creating the desired electrostatic interaction demands the deliberate design of catalytic structures and remains a grand challenge[4,21-23].

Herein, we discover that the electrostatically-accumulated Li^+ cations at the electrode/electrolyte interface can act as catalytic centers toward biomimetic aerobic oxygenation of ketones (Scheme 1). Bulk cations in solution are often surrounded by dipoles (e.g. H_2O in aqueous systems) or counter-ions (e.g. anions in non-polar solvents) via strong electrostatic interactions, which prevents the formation of desired electrostatic interactions with target substrates or intermediates. Therefore, these cations had been considered as bystanders or helpers and seldomly regarded as the catalytic centers[24-26], but the cations can universally accumulate at the electrode/electrolyte interface[27], which might create a unique microenvironment toward the desired electrostatic interactions that perform catalysis.

Results

Interfacial Li cations promote the aerobic electrochemical oxygenation of ketones.

The aerobic electrochemical oxygenation of ketones resembles the BVMO process and utilizes the reactive oxygen species from O_2 reduction for the sequential oxygenation with Baeyer Villiger (B-V) reactivity. We first screened different cations and discovered a dramatic difference among their catalytic performances (Figure 1a). In electrosynthesis systems, tetraalkylammonium salts (e.g. tetrabutylammonium (TBA)) are typically used to ensure the sufficient solubility and ionic conductivity. However, during the aerobic electrochemical oxygenation of cyclohexanone into ε-caprolactone (ε-CL), the TBA cations can only produce an ε-CL yield of 8.1% with a Faradaic efficiency of 13.0%. Shrinking the sizes of the ammonium cations can slightly

improve the yield but only to <15.0%. Interestingly, the use of 0.1 M lithium cations (Li^+) tremendously improved the ε-CL yield to 41.7% with a Faradaic efficiency of 67.1%, demonstrating catalytic behaviors.

Electrode material is another seminal component of the electrochemical system. Under the identical 0.1 M Li^+, carbon-based electrodes that favor the two-electron O_2 reduction outperformed the Pt/C electrode that encourages the four-electron O_2 reduction, suggesting the necessity of in-situ formed reactive oxygen species[28-31]. Among these carbon-based electrodes, multi-walled carbon nanotubes modified with carboxyl groups (CNT-COOH) exhibited the highest ε-CL yield, whereas other electrodes shared similar performances (Figure 1b). This was likely originated from the negative charges of the deprotonated carboxyl groups that encourage the accumulation of Li^+ cations (Scheme 1). Accordingly, CNT-COOH was utilized as the cathode, Li^+ and TBA^+ were utilized as representative cations in the following study.

According to the cyclic voltammetry (CV), the kinetics under Li^+ was greatly expedited with the shifted onset potential of O_2 reduction from -1.12 V vs. Fc^+/Fc under TBA^+ to -0.55 V vs. Fc^+/Fc (Figure 1c). In stark contrast to a pair of symmetrical single-electron O_2/O_2^- redox pair[32] under TBA^+, the Li^+ system showed the irreversible O_2 reduction toward more deeply-reduced oxygen species with the absence of the oxidation peak on the reversed scan. Considering the nature of Li^+, we speculate that the active species is likely anionic OOH^- that might form the short-range Li^+-OOH^- electrostatic interactions. Under O_2-free and H_2O_2 conditions, the Li^+ system demonstrated much negatively-shifted curves toward further H_2O_2 reduction and the

disappearance of the H_2O_2 oxidation compared to the TBA^+ system, corroborating the possible Li^+-OOH^- interaction.

The simplest method of enhancing the Li^+-mediated interactions is to increase the Li^+ concentrations. Increasing the Li^+ concentrations benefited the O_2 reduction current, but more importantly H_2O_2 oxidation was clearly present under 0.025 M Li^+ and disappeared beyond 0.1 M Li^+, indicating the more effective interaction under higher Li^+ concentrations (Figure 1d). This enhanced interaction led to an improved ε-CL yield to 60.1% under 0.8 M Li^+ that approaches saturation (Figure 1e). The time-dependent product analysis revealed that the reactions were mostly completed in 2700 s, and the general trend followed the higher yield and Faradaic efficiency under a higher Li^+ concentration. The Faradaic efficiency under a moderate Li^+ concentration of 0.2 M under 900 s could even reach 99.4%, while this value gradually diminishes over prolonging the electrolysis due to the consumed reactants for the insufficient consumption of O_2-reduction products.

Evidences of short-range Li^+-OOH^- interactions.

To verify our hypothesis of Li^+-OOH^- interactions, we first performed in situ surface-enhanced infrared absorption spectroscopy (SEIRAS) (Figure 2a and Figure S1). We could distinguish an O-O vibration peak at ~1124 cm^{-1} under Li^+ that gradually diminished under more negative potentials, accompanied by the evolving peak at ~1195 cm^{-1}. According to the simulated vibrations, the ~1124 cm^{-1} peak belongs to OOH^-, while the blue-shifted peak at ~1195 cm^{-1} corresponds to the Li^+-OOH^- complex (Figure

S2). On the contrary, the TBA^+ system showed the absence of vibrational peaks in this region, consistent with the CV observations (Figure S3). The in-situ surface-enhanced Raman spectroscopy (SERS) also confirmed the O-O stretching vibration of Li^+-OOH^- and OOH^- at 1193 cm^{-1} and 1092 cm^{-1}, respectively[33,34] (Figure 2b), and their absence under TBA^+ (Figure S4). There also existed the presence and absence of an O-O peak at 1011 cm^{-1} from the adsorbed O_2 state under Li^+ and TBA^+ respectively, resulting from the hydrophobic TBA^+ tail that traps the O_2 to prevent its adsorption on the electrode such that only the long-distance electron transfer can occur to generate O_2^-. The ultraviolet−visible (UV−vis) spectra of the cyclohexanone-free catholyte further confirmed the Li^+-OOH^- complex from the broad peak emerged at 273.3 cm^{-1} that shifted under different Li^+ concentrations (Figure S5-S6)[35]. After its accumulation, adding cyclohexanone with a 15-min reaction without applied potential could produce ε-CL (Figure S7), while no product could be detected without this accumulation (Figure S8), further demonstrating the catalytically-active Li^+-OOH^- species.

The configuration of the Li^+-OOH^- complex is key to its reactivity. The blue-shifted peaks in SEIRAS and SERS are intriguing, because if Li^+ attracts the terminal O of the OOH^- via electrostatic interaction, the O-O bond should be elongated to demonstrate a red-shifted vibration. Also, the terminal Li^+ can block the reactivity of OOH^-. Thus, we calculated the most thermodynamically-stable configuration of the Li^+-OOH^- complex as a side-on form with the three-center bonding (Figure 2c). The Li^+ drags the electrons from the p orbitals of the two O atoms to increase the O-O bond order, consistent with the observed blue-shifted vibrations. This stable side-on configuration facilitates the

formation of the Li^+-OOH^- complex. This was evidenced by the decreased dissociation energy of H_2O_2 from 9.26 eV without Li^+ and 8.31 eV under TBA^+ to 7.86 eV under Li^+, benefited from the more stable Li^+-OOH^- complex (Figure 2d). The O_2 reduction energy profiles with and without Li^+ on the CNT-COOH model were further calculated (Figure 2e and Figure S9). Despite the thermodynamically favorable O_2 reduction toward the H_2O end-product, the energy barrier from $^*OOH$ to $^*O$ demonstrates a high barrier of 1.18 eV, leaning toward the preferential H_2O_2 pathway often observed on carbon electrodes. Although the thermodynamic energy of Li^+-OOH^- is higher than H_2O_2, its kinetic barrier can be further reduced from 0.72 eV to 0.53 eV, favoring its production.

We further investigated the chemical property of this side-on Li^+-OOH^- complex by calculating the electrophilicity of each oxygen atom, using the orbital-weighted Fukui functions and condensed dual descriptor ($\Delta \boldsymbol{f}_{\boldsymbol{w}}$)[36] (Figure 2f). The formation of the cation-OOH^- interactions drastically decreases the $\Delta \boldsymbol{f}_{\boldsymbol{w}}$ values compared to bare OOH^-, corresponding to the increased nucleophilicity that benefits the oxygenation process. Additionally, the calculated Hirshfeld-charges reveal the significantly decreased Lewis basicity from OOH^- to TBA^+-OOH^- and further to Li^+-OOH^-. This diminished Lewis basicity enhanced the structural stability of the Li^+-OOH^- complex to prevent its protonation to form the more thermodynamically-stable but much less active H_2O_2. These results could be explained by the change in the electron density surrounding the terminal O atom (Figure 2c). The depletion of electron density away from the plane decreases the tendency of H_2O_2 formation, since this direction is

consistent with the more stable bent form of H_2O_2. Whereas, the increased electron density away from the Li^+ can still contribute to the enhanced nucleophilicity.

The determination of the active species allows us to elucidate the molecular-level B-V oxygenation mechanism (Figure 2g). Like other oxygenation systems, acetonitrile is a crucial mediator and creates a reactive adduct with a more favorable leaving group (Figure S10). Thus, the Li^+-OOH^- complex first nucleophilically attacks the acetonitrile to form the peroxyacetonitrile adduct (OOR^-), which can still form the short-range Li^+ interactions by Li^+-OOR^-. This complex can effectively attack the cyclohexanone to form a Criegee adduct, and two Criegee adducts are further coupled into a dimer with a lower energy barrier. This dimerization was supported by the significantly lower conversion and yield under lower cyclohexanone concentrations (Figure S11). The scission of the oxygen-oxygen bond in the dimer further forms a dioxy radical without much energy penalty, which can then be re-arranged to ε-CL as the final product. The dioxy radical can be evidenced by the absence of ε-CL under the DMPO-assisted radical trapping experiment (Figure S12).

The concept of effective Li^+ concentration and water-tolerance of Li^+-OOH^- complex.

Under 0.1 M Li^+, we could resolve the Li^+-OOH^- interaction from the CV, but no product was detected using H_2O_2 as the oxidant without applied potential. Due to the factors of the local electric field and incomplete dissociation of the salt, the bulk Li^+ concentration is not an effective indicator of its ability to form the Li^+-OOH^- complex

as well as the local Li^+ concentration at the interface. Consequently, we define the fractional concentration of Li^+ capable of forming Li^+-OOH^- complexes as the effective Li^+ concentration. A key parameter that affects the effective Li^+ concentration is the H_2O content. H_2O is a crucial component as the proton donor for the O_2 reduction into OOH^- and Li^+-OOH^- species, but can donate its dissociated protons to quench the active Li^+-OOH^- complex. Comparing the polarization curves under different H_2O contents demonstrated a distinct positive shift of potential upon H_2O addition (Figure 3a). Dosing beyond 5% H_2O led to the decreasing current at the first stage but the much-elevated current at ~-0.9 V vs. Fc^+/Fc, presumably corresponding to the deep O_2 reduction. Therefore, H_2O can be a double-edged sword that simultaneously benefited the kinetics of O_2 reduction and destroyed the desired Li^+-OOH^- complex via protonation to encourage deep reduction. Under 0.8 M Li^+, the positive shift was still present, but the change at 5% H_2O disappeared, suggesting the better water tolerance (Figure 3b). Accordingly, under 0.1 M Li^+, the ε-CL yield decreased from 41.2% of 0% H_2O to 21.7% of 1% H_2O, while under 0.8 M Li^+, the ε-CL yield was almost maintained, and only the excessive H_2O dosage led to further decreased yield (Figure 3c).

The time-dependent product analysis with different H_2O contents further confirmed the H_2O effect and H_2O-tolerance of 0.8 M Li^+ (Figure 3d). Under 900 s, dosing 1% H_2O increased the yield with a much-improved Faradaic efficiency to 99.6%, and further increasing H_2O ratios decreased yield and Faradaic efficiency. It suggested the essential role of H_2O for driving the O_2 reduction, but its overdosage quenches the active species. This quenching effect was further corroborated by the absence of O-O

vibration peaks of Li^+-OOH^- (1195 cm^{-1}) and OOH^- (1124 cm^{-1}) under 5% H_2O (Figure 3e). In all, the electrostatically-enriched Li^+ cations at the interface can serve as two major roles: 1) The under-coordinated Li^+ can effectively trap the in-situ generated OOH^- species to form the reactive side-on Li^+-OOH^- complex that mimics the active center of the BVMOs; 2) The excessive Li^+ in the surroundings can form the cation-dipole interaction with H_2O that prevents its donation of protons to destruct the Li^+-OOH^- complex, which in turn increases the effective Li^+ concentration. These Li^+ cations can act as an analogy to the NADPH cofactor that drags the N-H bond to prevent H_2O_2 formation (Scheme 1).

To further verify the Li^+/H^+ competition, we utilized the rotating ring disk electrode (RRDE) to measure the kinetics influenced by the reaction microenvironment. Theoretically, the reduction of O_2 to H_2O_2 or OOH^- involves the generation of 1 OH^- per e^- through a conventional proton-coupled electron transfer (PCET) process (eq. 1). However, the reduction of O_2 to Li^+-OOH^- with the H^+/Li^+ competition generates only one OH^- but transfers two electrons (eq.2).

$$O_2 + 2H_2O + 2e^- \rightarrow H_2O_2 + 2OH^- \quad \text{(eq.1)}$$

$$O_2 + H_2O + 2e^- + Li^+ \rightarrow Li^+\text{-}OOH^- + OH^- \quad \text{(eq.2)}$$

It could lead to a different proton/OH^- gradient at the interface. We cathodically biased the ring electrode to the hydrogen evolution potentials, and measured the kinetics differences with and without the O_2 reduction on the disk electrode. The larger current difference corresponds to the larger proton gradient. By comparing the scenarios of 0%

and 5% H_2O, we discovered that the system with 5% H_2O exhibited a much higher current difference and a faster current response of 346 mV/decade compared to 980 mV/decade with 0% H_2O (Figure 3f), corresponding to a higher proton gradient approaching the eq. 1 scenario with strong protonation tendency.

Another central factor that governs the effective Li^+ concentration is the Li^+-anion binding. In non-aqueous systems with low dielectric constants, Li^+-anion interaction can universally occur in solutions to encourage the dissolution[37,38], and these anions can compete with the OOH^-. The B-V oxygenation activity trend followed the order of $LiClO_4$<$LiBF_4$<LiTFSI<$LiPF_6$<LiFSI (Figure 3g), which is in coincidence with the calculated trend of the free energy of dissociation for different salts (Figure 3h). LiFSI can be spontaneously dissociated in acetonitrile and produces the highest ε-CL yield of 48.6% under 0.1 M, but its limited solubility in acetonitrile leads to its inferior activity under higher concentrations compared to $LiPF_6$. The O_2 reduction onset potential exhibited a consistent trend with ε-CL yield, with a more positive potential for the LiFSI, clearly indicating a promotion effect of the dissociated Li^+ (Figure 3i).

Quantitative description of the effective Li^+ under electrocatalysis and thermocatalysis.

Since the electrostatically-enriched Li^+ cations possess a much higher concentration at the interface than the bulk electrolyte, this difference in the effective cation concentration might be a key contributor to the observed oxygenation activity as well as the activity difference between electrocatalysis and thermocatalysis (Figure

S13). Therefore, we aimed to quantify this effective Li^+ concentration both at the interface and in the bulk. To mimic the bulk electrolyte scenario, we added H_2O_2 and Li^+-driven H_2O_2 dissociation into Li^+-OOH^- formed the active species. The addition of 0.025 M and 0.1 M $LiPF_6$ generated no ε-CL product and failed to compete with H^+ corresponding to a low effective Li^+ concentration (Figure 4a). Comparatively, modest yields of ε-CL could be obtained under the electrostatically-enriched Li^+ at the electrode/electrolyte interface. We only observed ε-CL production under H_2O_2 beyond 0.2 M Li^+. Interestingly, the ε-CL yield under H_2O_2 with 0.8 M Li^+ was almost equivalent to that under electrochemical O_2 reduction with 0.1 M Li^+. It might indicate that assuming similar microenvironments near the vicinity of Li^+, the concentration of electrostatically-enriched cations was ~ 8 times higher than the bulk concentration.

However, the direct quantification of the effective Li^+ still remains to be solved. Since the spectroscopic signal of the Li^+-OOH^- is not well-defined and affected by solvent species, we utilized an azide (N_3^-) probe to mimic the OOH^- anion. The infrared N_3^- vibrations have well-defined peaks with negligible background interference, and the short-range Li^+-N_3^- interaction could also cause a shift in the N_3^- vibrational peak, allowing for the quantification of their relative abundance. The SEIRAS spectra in 0.1 M Li^+ at -0.5 V vs. Fc^+/Fc near open-circuit potential (OCP) resembles the thermocatalytic condition. Two major vibration peaks of ~2110 cm^{-1} from the Li^+-N_3^- and ~2080 cm^{-1} from the solvated N_3^- appeared at this potential (Figure 4b and Figure S14). After applying -1.5 V vs. Fc^+/Fc, an additional peak at 2148 cm^{-1} emerged, corresponding to the N_3^- coordinated to multiple Li^+ (nLi^+-N_3^-) (Figure S14). This was

likely originated from the relatively low solubility of LiN_3 solid and high Li^+ to N_3^- ratio used (0.1 M Li^+ vs. <0.01 M N_3^-). Under 0.8 M Li^+, an apparent peak at 2180 cm^{-1} was observed even at OCP, and this more blue-shifted peak was likely attributed to the LiN_3 crystallites that contain the multiple Li^+-N_3^- coordination. Biasing the system to -1.5 V vs. Fc^+/Fc recovered to three major peaks at 2147 cm^{-1}, 2104 cm^{-1} and 2078 cm^{-1} (Figure 4c). The well-defined peak shapes allowed the quantification of the relative proportions of these species near OCP that represents the bulk electrolyte under thermocatalytic conditions and -1.5 V vs. Fc^+/Fc that represents the interface under electrocatalytic conditions (Figure 4d and 4e). Under thermocatalytic conditions, the major component is the solvated N_3^- with negligible contribution of nLi^+-N_3^-, while extending beyond 0.2 M Li^+ significantly increased the proportions of nLi^+-N_3^- and Li^+-N_3^-. Under 0.8 M Li^+, the relative proportion of nLi^+-N_3^- could reach 17.35%. Under electrocatalytic conditions, a significant proportion of 16.12% for nLi^+-N_3^- was present even in 0.1 M Li^+, which further increased to 38.6% under 0.8 M Li^+.

We then used the Kendall correlation coefficient to illustrate the relevance of this quantification with B-V oxygenation activity (Figure 4f and 4g). The correlation coefficient based on the proportion of nLi^+-N_3^- was the highest among all three species, and further including the Li^+-N_3^- did not benefit the coefficient, suggesting the central species of nLi^+-N_3^-. It is worthwhile to emphasize that the relative solubility differences between LiN_3 and LiOOH may give rise to the difference in the coordination environment of Li^+ to N_3^- and OOH^-, but this correlation still raises the attention to the possible active anionic species coordinated to multiple cations due to the highly-

concentrated cations at the electrode interface. Another important evidence is that the proportion of nLi^+-N_3^- under 0.8 M Li^+ and thermocatalytic conditions is 17.35%, very close to the 16.12% under 0.1 M Li^+ and electrocatalytic conditions. This was highly consistent with the trend of the ε-CL yield, indicating that we might successfully quantify the effective Li^+ concentration via the N_3^--assisted method. Under 0.1 M bulk concentration, no effective Li^+ with undercoordination characteristics could be obtained in the bulk, while the effective ratio could reach <20% at the interface, while this value could only be achieved for the bulk by octupling the Li^+ concentration.

The differences in the thermocatalytic and electrocatalytic systems could be extended to other Li^+ salts, such as LiFSI and LiTFSI (Figure 4h and S15). The LiFSI showed a similar trend compared to $LiPF_6$, but due to its low solubility, the ε-CL began to be thermocatalytically produced from a lower concentration of 0.1 M, likely owing to the more facile formation of Li^+ complexes near the crystallite surface. However, increasing the LiFSI concentration was not beneficial for the electrocatalytic condition, because the Li^+ cations already formed a near-saturation interface while increasing the concentration of crystallites did not necessarily accumulate at the interface. In contrast, LiTFSI showed the opposite trend. It has a relatively higher solubility such that the electrocatalytic trend was similar to $LiPF_6$, but no product was detected under thermocatalytic conditions, even at very large concentrations. The Li^+ and $TFSI^-$ facilely formed Li^+-$TFSI^-$ ion pairs, which buried the Li^+ and prevented the formation of active complexes, while the applied electric field pulled away the ion pairs to construct the Li^+-accumulated interface and allowed the formation of active Li^+ species.

Overall, this strategy of creating the electrostatically-accumulated ion interfaces to modulate the nature and concentration of active species is highly effective, and also shines light on the intrinsic differences and similarities of chemo-reactivity in electrocatalytic and themocatalytic systems. This strategy and relevant analysis could be further extended to the oxygenation of other ketone systems, especially the highly resembled activities of 0.1 M Li^+/electrocatalysis and 0.8 M Li^+/thermocatalysis, and can provide a reference for other ion-sensitive systems (Figure 4i).

Discussion

Herein, by simulating the unique electrostatic interaction in BVMO enzymes, we discovered that the electrostatically-enriched Li^+ cations can efficiently catalyze the aerobic oxygenation of ketones. Through systematic optimization, we demonstrated that the effective accumulation of Li^+ cations induced by the applied potential and carboxylated carbon nanotube electrodes can generate a high yield of 60.1% and a Faradaic efficiency of 64.42% for the representative cyclohexanone oxidation. The enriched Li^+ cations can not only induce short-range electrostatic interactions with the OOH^- intermediate generated by the electrochemical O_2 reduction, but also attract water dipoles to prevent the annihilation of the active Li^+-OOH^- complex. Kinetic analysis, in-situ spectroscopy, and DFT calculations reveal that the side-on Li^+-OOH^- complex can effectively reduce the energy barrier of O_2 reduction and increase the nucleophilicity toward oxygenation. The competition of the Li^+-OOH^- complex with

the proton source and anionic species was highly critical for the activity, which led to the concept of effective Li^+ at the interface that facilely form the Li^+-OOH^- complex. The effective Li^+ concentration behaves very differently at the electrode/electrolyte interface and in the bulk solution. This difference accounts for the observed distinction between electrocatalysis and thermocatalysis. By using the N_3^- probe-assisted method, we quantified the effective Li^+ fraction that can facilely form short-range electrostatic interactions with anionic species, and revealed that the electrostatically-enricheded Li^+ cations are more effective than the bulk Li^+ cations for creating desired electrostatic interactions, by a factor of up to 8. This discrepancy shines light on the intrinsic chemoreactivity difference in electrocatalysis and thermocatalysis, and this work points to the prospective route of utilizing electrostatically-enriched ions for the efficient catalytic transformation, especially toward the synthesis of fine chemicals.

Online Method

Chemicals. All reagents were used as received without further purification. Cyclohexanone ($C_6H_{10}O$, Standard for GC), ε-caprolactone ($C_6H_{10}O_2$, 99%), cyclobutanone (C_4H_6O, 99%), cyclopentanone (C_5H_8O, >99.0%), lithium hexafluorophosphate ($LiPF_6$, 97%), ammonium hexafluorophosphate (NH_4PF_6, 99.99%), tetramethylammonium hexafluorophosphate ($C_4H_{12}F_6NP$, 98%), platinum on carbon (Pt, 5 wt. %), tetraethylammonium hexafluorophosphate ($C_8H_{20}F_6NP$, 98%), tetrabutylphosphonium hexafluorophosphate ($C_{16}H_{36}F_6P_2$, 98%), isopropyl alcohol

(C_3H_8O, 99%), lithium perchlorate trihydrate ($LiClO_4 \cdot 3H_2O$, 99.99%), bis(trifluoromethane)sulfonimide lithium salt ($C_2F_6LiNO_4S_2$, 99%), fumaric acid ($C_4H_4O_4$, ≥99.5%), lithium azide solution (LiN_3, 20 wt. % in H_2O), 5,5-dimethyl-1-pyrroline N-oxide ($C_6H_{11}NO$, 97%), deuterium oxide (D_2O, 99.9 atom % D), hydrogen peroxide solution (H_2O_2, AR, 30 wt. % in H_2O), lithium tetrafluoroborate ($LiBF_4$, 99.99%), silver nitrate ($AgNO_3$, 99.8%), lithium bis(fluorosulfonyl)imide ($F_2LiNO_4S_2$, >98.0%), ferrocene ($FeC_{10}H_{10}$, 99%) were purchased from Aladdin Industrial Corporation (China). Acetonitrile (CH_3CN, ≥ 99.0%) was purchased from Sinopharm Chemical Reagent Co., Ltd. (China). Carbon fiber paper was purchased from Hesen Electric Co., Ltd. (HCP020P, China). Carbon black was purchased from Shanghai Lisheng Industrial Co., Ltd. Nanographite powder was purchased from Sigma-Aldrich Trading Co., Ltd. Graphene sheets were purchased from TCI Chemical Industrial Development Co., Ltd. Carboxyl carbon nanotubes and carbon nanotubes were purchased from Beijing Deke Island Gold Technology Co., Ltd. Pt sheets, glassy carbon electrode and Ag^+/Ag electrodes were purchased from Wuhan GaossUnion Technology Co., Ltd. (China). Ultrapure Deionized water (18.2 MΩ·cm^{-1}, 25 °C) was obtained from ELGA Purification system (China).

Catalyst Electrode Preparation. Carbon paper (1 cm × 1 cm × 0.1 cm) were ultrasonically washed with deionized water and ethanol to remove surface contaminants. Prepare ink by dispersing 4 mg catalyst in 1000 μL isopropyl alcohol with 20 μL Nafion. The resulting mixture was then sonicated for 20 min to obtain a uniform ink. Finally, 250μL of ink was dropped on hydrophobic carbon paper and dried at 80 °C. After the

glassy carbon electrode was polished with polishing powder, it was ultrasonicated in water for 10 min, ultrasonicated in ethanol for 10 min, and dried naturally at room temperature. The electrochemical workstation (CHI 660E, Shanghai CH Instruments Co., China) was used for the potential control.

Electrochemical measurements. The electrochemical measurements were performed on a CHI 660E work station using a standard 5 mL electrochemical cell with a three-electrode system. The as-prepared electrodes were directly served as the working electrode. A Pt sheet and an Ag^+/Ag electrode in 0.1 M $AgNO_3$ were used as the counter electrode and the reference electrode, respectively. All measured potentials in our work were converted to Fc^+/Fc scale. The kinetics study was examined by polarization curves/cyclic voltammetry curves under a scan rate of 100 mV/s, corrected with 80% iR-compensation. In the electrocatalytic oxidation of ketone experiment, we applied a constant current in 60 mM ketone + x M salt (x = 0.025, 0.1, 0.2, 0.4, 0.8) + acetonitrile for 2700 s. During the electrolysis process, the oxygen in the system is always saturated. In addition, acetonitrile was continuously added to the system through a peristaltic pump to keep the volume constant. All experiments were conducted at a room temperature of 25 °C.

Electrolysis product analysis. Product Analysis. The products were analyzed by nuclear magnetic resonance (NMR, Bruker 400 MHz Avance III HD) spectrometer. The ε-CL product was quantified by ^1H NMR with fumaric acid as the internal standard. The standard method includes adding 100 μL electrolyte into a 400 μL D_2O solution with 100 μL 0.01 M fumaric acid. The number of moles of the product ($n_{\varepsilon\text{-CL}}$) was

calculated using the following equation.

$$n_{\varepsilon-\mathrm{CL}} = \frac{A_{\varepsilon-\mathrm{CL}} \times N_{\text{fumaric acid}}}{A_{\text{fumaric acid}} \times N_{\varepsilon-\mathrm{CL}}} \times n_{\text{fumaric acid}}$$

where $A_{\text{ε-CL}}$ is the integral area of the ε-CL peak (4.35 ppm) in the NMR spectrum (Figure S13), which corresponds to two protons, $N_{\text{ε-CL}}$ is the corresponding H number ($N_{\text{ε-CL}}$ = 2). $A_{\text{fumaric acid}}$ is the integral area of the fumaric acid peak (6.70 ppm), and $N_{\text{fumaric acid}}$ is the corresponding H number ($N_{\text{fumaric acid}}$ = 2) of the fumaric acid peak. The yield of the product was calculated by the following equations.

$$\text{yield}_{\varepsilon-\mathrm{CL}} = \frac{n_{\varepsilon-\mathrm{CL}}}{n_{\text{cyclohexanone}}} \times 100\%$$

Where $n_{\text{ε-CL}}$ is the mole number of ε-CL and $n_{\text{cyclohexanone}} = 3 \times 10^{-4}$ is the initial mole number of the cyclohexanone.

The product faradaic efficiency (FE) was calculated by the following equation.

$$\mathrm{FE}_{\varepsilon-\mathrm{CL}} = \frac{n_{\varepsilon-\mathrm{CL}} z_{\varepsilon-\mathrm{CL}} \mathrm{F}}{Q_{total}} \times 100\%$$

Where $z_{\text{ε-CL}}$ = 4 is the number of electrons required to produce a ε-CL, F is the faradaic constant (96,485 C/mol), and Q_{total} is the total charge.

UV-Vis and *In-situ* ATR-SEIRAS spectroscopy. UV-vis spectroscopic measurements were performed using a UV-vis spectrometer (Lambda 35, PerkinElmer). The UV-vis spectrometer was referenced to deionized water using a quartz cuvette. UV-vis spectra of the electrolyte were measured at different reaction stages on the carboxy carbon tube with $LiPF_6$. After electrolysis for 0/5/10/15 min, The electrolyte in the cathode part of the H-type cell is used in UV-visible spectrophotometers measurement.

UV-vis spectroscopy characterization studies were conducted on various concentrations of $LiPF_6$ in x M $LiPF_6$ (x = 0.025, 0.1, 0.8) for 5 min.

Since the focus is on the electrode interface rather than the catalyst, We directly used Au disk electrode (Φ = 10 mm) as our working electrode. The ATR-SEIRAS spectra were collected by a Nicolet iS20 FTIR spectrometer (Nicolet iS20 FTIR, Thermo Scientific) with a built-in MCT detector and an in-situ IR optical accessory (SPEC-I, Shanghai Yuanfang Tech. Co., Ltd., China). The Au-coated Si prism was used as the working electrode, with the Ag^+/Ag electrode and the Pt foil as the reference and counter electrodes, respectively. Potentio-dynamic measurement was conducted in the N_2-saturated atmosphere, and ~10 sccm N_2 flow was kept bubbling through the spectro-electrochemical cell and infrared spectrometer. ATR spectra were acquired at a resolution of 4 cm^{-1} with unpolarized IR radiation at an incidence angle of ca. 60°. All spectra were converted to the absorbance unit as -log (I/I_0), where I and I_0 represent the signal intensities of the reflected radiation of the sample and reference spectra. The electrochemical workstation (CHI 660E, Shanghai CH Instruments Co., China) was utilized for the potential control.

Rotating ring disk electrode test (RRDE). After polishing the rotating ring disk electrode with polishing powder, it was ultrasonicated in water for 3 min, in ethanol for 3 min, and dried naturally at room temperature. Prepare the ink by dispersing 2 mg of catalyst in 700 μL of water, 300 μL of isopropyl alcohol, and 20 μL of Nafion. The resulting mixture was then sonicated for 20 minutes to obtain a uniform ink. Finally, 10 μL of ink was dropped on the disk electrode and dried at room temperature. The kinetics

study was examined by polarization curves under a scan rate of 10 mV/s, corrected with 80% iR-compensation. The electrochemical workstation (CHI 760E, Shanghai CH Instruments Co., China) was utilized for the potential control.

***In-situ* Raman spectroscopic study.** The Raman spectra were recorded by Raman spectrometer (Horiba Jobin Yvon) equipped with a 638 nm laser. The spectral Raman shift range was set from 200 to 2000 cm^{-1} with the resolution of 1.3 cm^{-1}, using a 1200/mm grating and setting the acquisition time as 60 s. The Raman spectroscopy was conducted on a custom-built three-electrode cell (EC-RAIR, Beijing Science Star technology Co., Ltd.), with the Pt wire as the counter electrode, the Ag/Ag^{+} electrode as the reference electrode (0.1 M $AgNO_3$) and a roughened gold surface as the working electrode. The Au electrode for the in-situ Raman spectroscopic study was prepared by a modified electrodeposition method on the roughened gold electrode. The electrodeposition was conducted at a current density of 1 $mA \cdot cm^{-2}$ with a deposition duration of 120 s. The working electrode was further washed with ultrapure deionized water and ethanol. Before the spectroscopic study, the electrode is immersed in a saturated solution of O_2. The Raman spectrum is collected by sweeping the electrode over a specified potential range.

Calculation Details. The density functional theory (DFT) calculations of Oxygen reduction reaction (ORR) processes on the anode of multi-walled carbon nanotubes modified with carboxyl groups (CNT-COOH) were performed in the framework of periodic plane waves implemented in the Vienna ab initio simulation package (VASP, version 5.4.4, https://www.vasp.at) The electron-ion interactions are represented by

projector-enhanced waves (PAW)[39], and the energy cut-off is 440 eV using the PBE function. The VASPsol package was also imported corrections of DFT-D3 and solvation in acetonitrile (EB_K= 35.69 F/m). As the CNT-COOH in our practical experiment is in relatively large radius, causing its curvature can be ignored at the nanoscale, the CNT models with -COOH function groups on the basal (CNT-COOH-Basal) and at the edge (CNT-COOH-edge) were both formed flat[40], as shown in Figure S9. For geometrical optimization, the convergence criterion for forces acting on atoms is 0.02 eV•Å^{-1}, while the energy threshold defining the self-consistency of the electron density is 10^{-6} eV.

DFT calculations of B-V oxygenation process and other cluster structures were performed using the Gaussian 16 rev. b.01 suite of programs (https://gaussian.com). Application of the TPSSh function in combination with 6-311+G(d, p) basis set was used for the analysis of the Fukui functions and electron density distribution; the M062X functional in combination with the def2-tzvp basis set was used for the geometry optimizations and frequency computations of intermediate-/end-products and transition states, with correction of DFT-D3[41]; the calculations of IR spectra was calculated at B3LYP/6-31G(d) level with correction factor of 0.9614[42]. The whole DFT calculations were performed under in acetonitrile solution by using IEFPCM method. We have employed unrestricted M062X methods and found broken-symmetry solutions for the open-shell triplet. For each transition-state, IRC calculations were performed in both directions to locate the nearest stationary points; the resulting structures were subjected to geometry optimization and frequency calculations. Multiwfn (http://sobereva.com/multiwfn/) was imported for the electronic wavefunction

analysis[43].

Date availability

The data that support the findings of this study are available from the corresponding author upon reasonable request.

Acknowledgement

This work was financially supported by the Shanghai Technology Innovation Program (Carbon-Neutral Program, 21DZ1207800, Technical Center, 20DZ2250600), the Shanghai Pujiang Program (21PJD016), the National Natural Science Foundation of China (Nos. 22172036, 21876049 and 22222602), the National Key Research and Development Program of China (No. 2019YFA0705800).

Author contributions

X. Y. and M. G. conceived the idea, designed the research project and co-wrote the manuscript. S. C. performed the experiments, collected and analyzed the data and co-wrote the manuscript. Y. Y. contributed to the computational results and co-wrote the manuscript. W. D., T. J., R. W., M. Q., Z. J. and C. Y. helped to analyze the data and write the manuscript. All the authors discussed the results and commented on the paper.

References

1 Jin, M. Y. *et al.* Engineered non-covalent π interactions as key elements for chiral recognition. *Nature Communications* **13**, 3276 (2022).

2 Laconsay, C. J., Seguin, T. J. & Wheeler, S. E. Modulating Stereoselectivity through Electrostatic Interactions in a SPINOL-Phosphoric Acid-Catalyzed Synthesis of 2, 3-Dihydroquinazolinones. *ACS Catalysis* **10**, 12292-12299 (2020).

3 Robiette, R., Trieu-Van, T., Aggarwal, V. K. & Harvey, J. N. Activation of the SN_2 reaction by adjacent π systems: the critical role of electrostatic interactions and of dissociative character. *Journal of the American Chemical Society* **138**, 734-737 (2016).

4 Neel, A. J., Hilton, M. J., Sigman, M. S. & Toste, F. D. Exploiting non-covalent π interactions for catalyst design. *Nature* **543**, 637-646 (2017).

5 Maji, R., Mallojjala, S. C. & Wheeler, S. E. Electrostatic Interactions in Asymmetric Organocatalysis. *Accounts of Chemical Research* **56**, 1990-2000 (2023).

6 Yi, J. *et al.* Electrostatic interactions accelerating water oxidation catalysis via intercatalyst O-O coupling. *Journal of the American Chemical Society* **143**, 2484-2490 (2021).

7 Zhan, S., Zhang, B., Sun, L. & Ahlquist, M. S. Hydrophobic/hydrophilic directionality affects the mechanism of Ru-catalyzed water oxidation reaction. *ACS Catalysis* **10**, 13364-13370 (2020).

8 Huang, Z. *et al.* Anion-π interactions suppress phase impurities in $FAPbI_3$ solar cells. *Nature* **623**, 531-537 (2023).

9 Perras, F. A., Marion, D., Boisbouvier, J., Bryce, D. L. & Plevin, M. J. Observation of CH···π interactions between methyl and carbonyl groups in proteins. *Angewandte Chemie International Edition* **129**, 7672-7675 (2017).

10 Kilgore, H. R. & Raines, R. T. n→ π* interactions modulate the properties of cysteine residues and disulfide bonds in proteins. *Journal of the American Chemical Society* **140**, 17606-17611 (2018).

11 Getzoff, E. D. *et al.* Electrostatic recognition between superoxide and copper, zinc superoxide dismutase. *Nature* **306**, 287-290 (1983).

12 Coulther, T. A., Ko, J. & Ondrechen, M. J. Amino acid interactions that facilitate enzyme catalysis. *The Journal of Chemical Physics* **154** (2021).

13 Benkovic, S. J. & Hammes-Schiffer, S. A perspective on enzyme catalysis. *Science* **301**, 1196-1202 (2003).

14 Romney, D. K., Colvin, S. M. & Miller, S. J. Catalyst control over regio-and enantioselectivity in Baeyer-Villiger oxidations of functionalized ketones. *Journal of the American Chemical Society* **136**, 14019-14022 (2014).

15 Maalouf, J. H., Jin, K., Yang, D., Limaye, A. M. & Manthiram, K. Kinetic analysis of electrochemical lactonization of ketones using water as the oxygen atom source. *ACS Catalysis* **10**, 5750-5756 (2020).

16 Ma, Q., Xing, W., Xu, J. & Peng, X. Baeyer-Villiger oxidation of cyclic ketones with aqueous hydrogen peroxide catalyzed by transition metal oxides. *Catalysis*

Communications **53**, 5-8 (2014).

17 Fürst, M. J., Gran-Scheuch, A., Aalbers, F. S. & Fraaije, M. W. Baeyer-Villiger monooxygenases: tunable oxidative biocatalysts. *ACS Catalysis* **9**, 11207-11241 (2019).

18 Corma, A., Nemeth, L. T., Renz, M. & Valencia, S. Sn-zeolite beta as a heterogeneous chemoselective catalyst for Baeyer-Villiger oxidations. *Nature* **412**, 423-425 (2001).

19 Fürst, M. J. *et al.* Polycyclic ketone monooxygenase from the thermophilic fungus Thermothelomyces thermophila: a structurally distinct biocatalyst for bulky substrates. *Journal of the American Chemical Society* **139**, 627-630 (2016).

20 Yachnin, B. J., Sprules, T., McEvoy, M. B., Lau, P. C. & Berghuis, A. M. The substrate-bound crystal structure of a Baeyer-Villiger monooxygenase exhibits a Criegee-like conformation. *Journal of the American Chemical Society* **134**, 7788-7795 (2012).

21 Hastings, C. J., Pluth, M. D., Bergman, R. G. & Raymond, K. N. Enzymelike catalysis of the Nazarov cyclization by supramolecular encapsulation. *Journal of the American Chemical Society* **132**, 6938-6940 (2010).

22 Ren, X. *et al.* Microenvironment engineering of ruthenium nanoparticles incorporated into silica nanoreactors for enhanced hydrogenations. *Angewandte Chemie International Edition* **58**, 14483-14488 (2019).

23 Li, X. *et al.* Microenvironment modulation of single-atom catalysts and their roles in electrochemical energy conversion. *Science Advances* **6**, eabb6833 (2020).

24 Li, X. Y. *et al.* Mechanism of cations suppressing proton diffusion kinetics for electrocatalysis. *Angewandte Chemie International Edition* **62**, e202218669 (2023).

25 Yang, X. *et al.* Cation-Induced Interfacial Hydrophobic Microenvironment Promotes the C-C Coupling in Electrochemical CO_2 Reduction. *Journal of the American Chemical Society* (2024).

26 Qin, X., Hansen, H. A., Honkala, K. & Melander, M. M. Cation-induced changes in the inner-and outer-sphere mechanisms of electrocatalytic CO_2 reduction. *Nature Communications* **14**, 7607 (2023).

27 Gebbie, M. A., Liu, B., Guo, W., Anderson, S. R. & Johnstone, S. G. Linking Electric Double Layer Formation to Electrocatalytic Activity. *ACS Catalysis* **13**, 16222-16239 (2023).

28 Gong, L. *et al.* Marriage of ultralow platinum and single-atom MnN_4 moiety for augmented ORR and HER catalysis. *ACS Catalysis* **13**, 4012-4020 (2023).

29 Zhang, C. *et al.* A pentagonal defect-rich metal-free carbon electrocatalyst for boosting acidic O_2 reduction to H_2O_2 production. *Journal of the American Chemical Society* **145**, 11589-11598 (2023).

30 Bu, Y. *et al.* Carbon-based electrocatalysts for efficient hydrogen peroxide production. *Advanced Materials* **33**, 2103266 (2021).

31 Lim, J. S. *et al.* Designing highly active nanoporous carbon H_2O_2 production electrocatalysts through active site identification. *Chem* **7**, 3114-3130 (2021).

32 AlNashef, I. M., Leonard, M. L., Kittle, M. C., Matthews, M. A. & Weidner, J. W. Electrochemical generation of superoxide in room-temperature ionic liquids. *Electrochemical and Solid-State Letters* **4**, D16 (2001).

33 Peng, Z., Chen, Y., Bruce, P. G. & Xu, Y. Direct detection of the superoxide anion as a stable intermediate in the electroreduction of oxygen in a non-aqueous electrolyte

containing phenol as a proton source. *Angewandte Chemie International Edition* **127**, 8283-8286 (2015).

34 Huang, S. *et al.* Well-defined N_3C_1-anchored Single-Metal-Sites for Oxygen Reduction Reaction. *Angewandte Chemie International Edition* **63**, e202314833 (2024).

35 Chlistunoff, J. & Simonin, J.-P. Ionic association of hydroperoxide anion HO_2^- in the binding mean spherical approximation. Spectroscopic study of hydrogen peroxide in concentrated sodium hydroxide solutions. *The Journal of Physical Chemistry A* **110**, 13868-13876 (2006).

36 Pino-Rios, R., Inostroza, D., Cárdenas-Jirón, G. & Tiznado, W. Orbital-weighted dual descriptor for the study of local reactivity of systems with (quasi-) degenerate states. *The Journal of Physical Chemistry A* **123**, 10556-10562 (2019).

37 Chen, X. & Zhang, Q. Atomic insights into the fundamental interactions in lithium battery electrolytes. *Accounts of Chemical Research* **53**, 1992-2002 (2020).

38 Chen, X., Zhang, X. Q., Li, H. R. & Zhang, Q. Cation-solvent, cation-anion, and solvent-solvent interactions with electrolyte solvation in lithium batteries. *Batteries & Supercaps* **2**, 128-131 (2019).

39 Kresse, G. & Joubert, D. From ultrasoft pseudopotentials to the projector augmented-wave method. *Physical review b* **59**, 1758 (1999).

40 Lu, Z. *et al.* High-efficiency oxygen reduction to hydrogen peroxide catalysed by oxidized carbon materials. *Nature Catalysis* **1**, 156-162 (2018).

41 Moellmann, J. & Grimme, S. DFT-D3 study of some molecular crystals. *The Journal of Physical Chemistry C* **118**, 7615-7621 (2014).

42 Scott, A. P. & Radom, L. Harmonic vibrational frequencies: an evaluation of Hartree-Fock, Møller-Plesset, quadratic configuration interaction, density functional theory, and semiempirical scale factors. *The Journal of Physical Chemistry* **100**, 16502-16513 (1996).

43 Lu, T. & Chen, F. Multiwfn: A multifunctional wavefunction analyzer. *Journal of computational chemistry* **33**, 580-592 (2012).

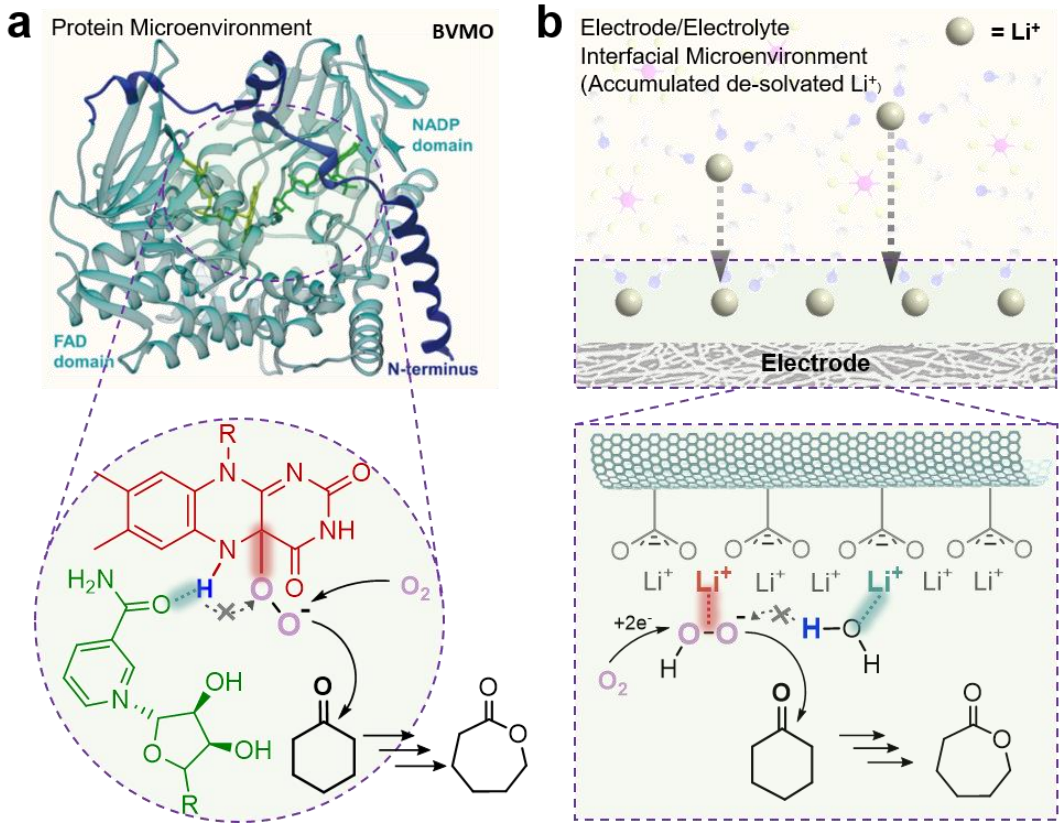

Scheme 1. (a) The mechanism of BVMO enzyme[17]. (b) Biomimetic mechanism of aerobic oxygenation by electrostatically-enriched Li^+.

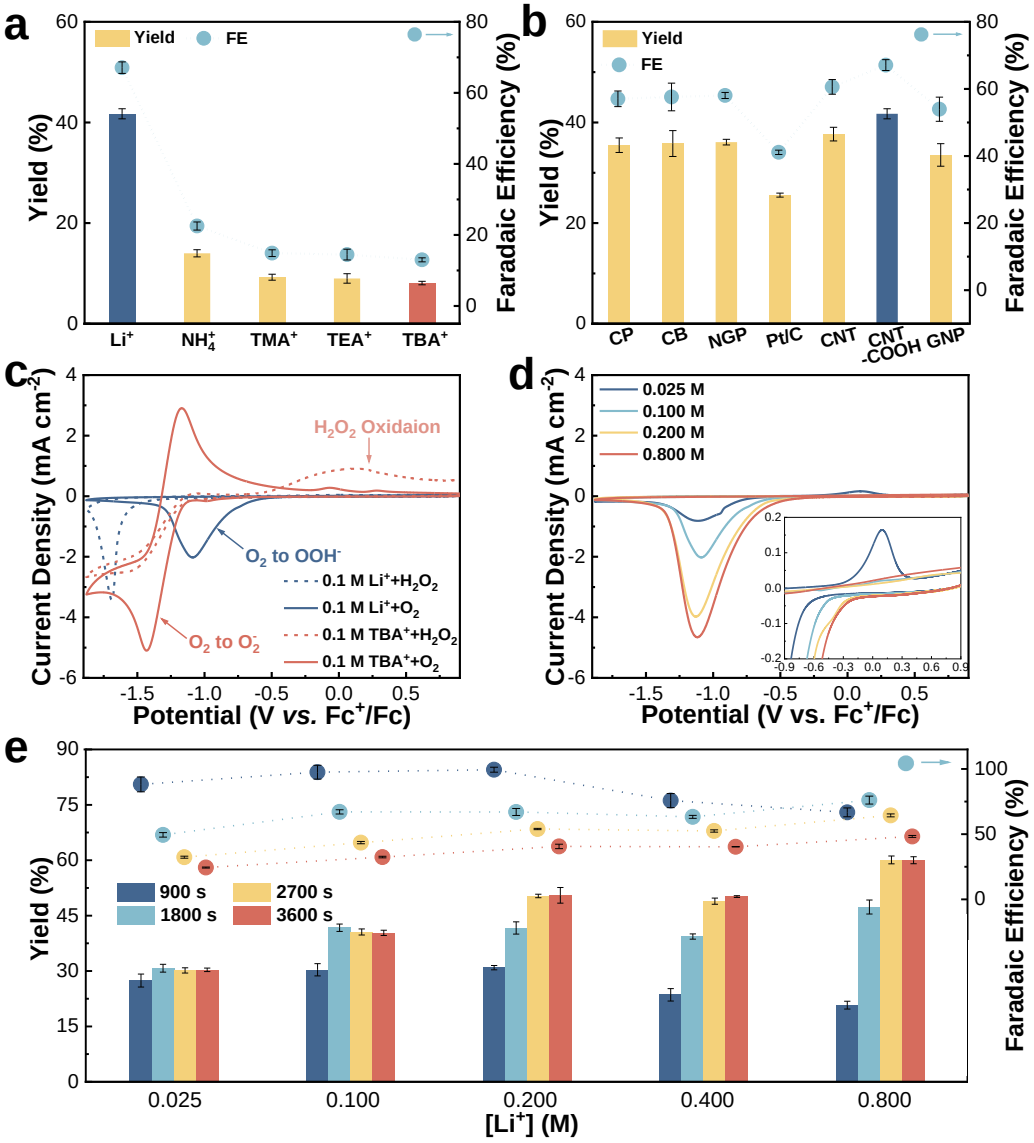

Figure 1. a) The yield/Faradaic efficiency of ε-CL with different cations. b) The yield/Faradaic efficiency of ε-CL on different catalyst electrodes under 0.1 M $LiPF_6$. c) Cyclic voltammetry curves of O_2/H_2O_2 reduction under Li^+ or TBA^+ on a glassy carbon electrode. The scan rate is 100 mV/s. d) Cyclic voltammetry curves of O_2 reduction on a glassy carbon electrode under different concentrations of $LiPF_6$. The scan rate is 100 mV/s. e) Time-dependent ε-CL yield/Faradaic efficiency under different concentrations of $LiPF_6$.

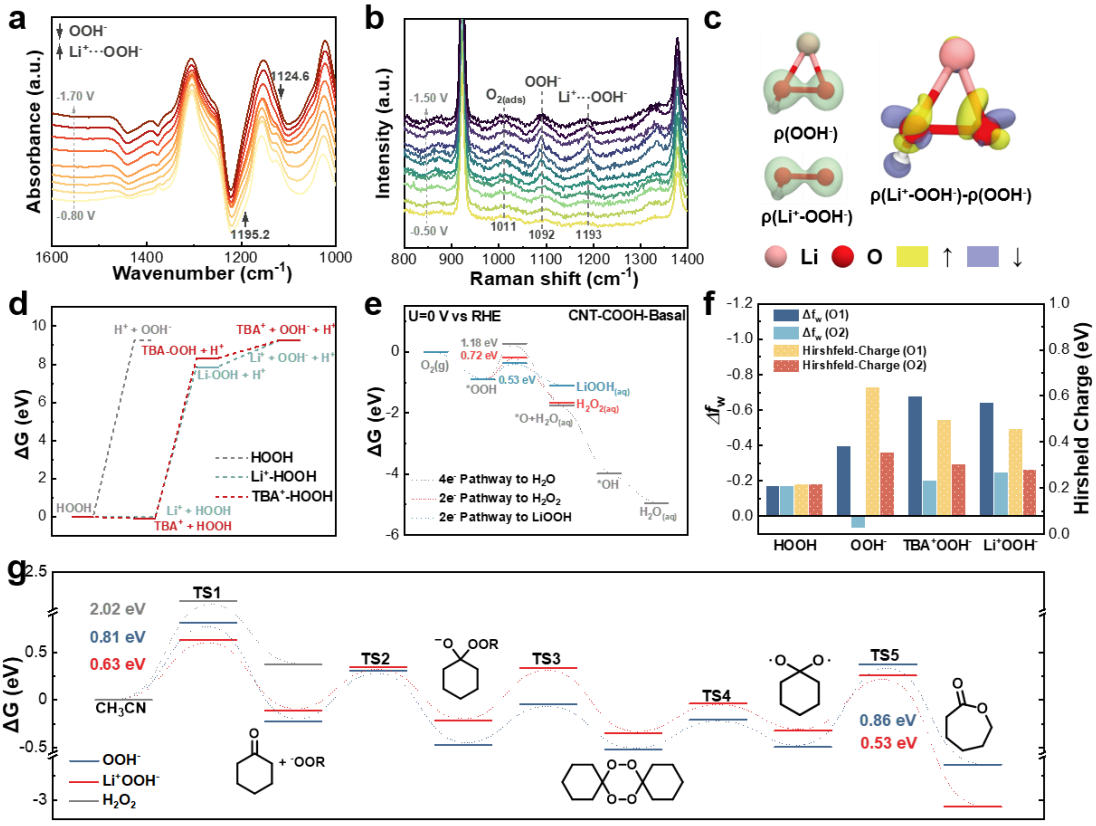

Figure 2. a-b) The ATR-SEIRAS/in-situ SERS spectra of the system when polarized to different potentials in an electrolyte with Li^+ under O_2. c) Calculated electron density and their difference of Li^+-OOH^- complex and OOH^- anion (value = 0.007 a. u., blue represents a decrease in the electron density, yellow represents the opposite). d) Energy transition of H_2O_2 dissociation with or without cation coordination. e) Energy profile of O_2 reduction with and without Li^+ on the CNT-COOH-Basal model. f) The electrophilicity of each oxygen atom on H_2O_2 and OOH^- with/without cationic coordination described by orbital weighted Fukui functions and condensed duality descriptors (O1 represents the O atom away from the H and O_2 represents the O atom close to the H. g) The Gibbs free energy distribution of the cyclohexanone oxygenation pathway.

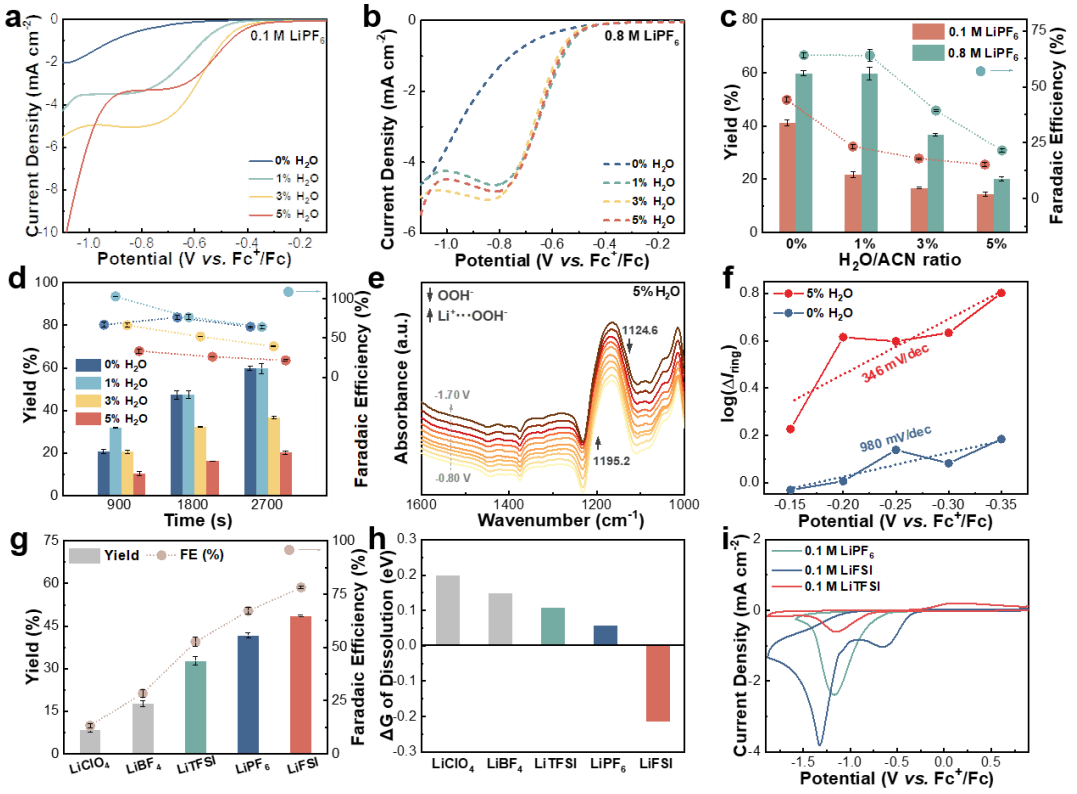

Figure 3. a-b) Polarization curves of O_2 reduction in a) 0.1 M and b)0.8 M $LiPF_6$ system with different H_2O contents. c) The yield and Faradaic efficiency of ε-CL in 0.1/0.8 M $LiPF_6$ system with different H_2O contents. d) Time-dependent ε-CL yield/Faradaic efficiency under different H_2O contents under 0.8 M $LiPF_6$. e) The ATR-SEIRAS spectra of the system when polarized to different potentials in 0.1 M $LiPF_6$ system with 5% H_2O. f) The current difference of the Pt ring electrode at different potentials under the influence of 41 μA/cm^2 and 2.57 mA/cm^2 the disk electrode in 0.1 $LiPF_6$ system. g) The yield and Faradaic efficiency of ε-CL in Li salt systems with different anions. h) Calculated Gibbs energies of dissolution for Li salts with different anions. i) Polarization curves of O_2 reduction under Li salts with different anions.

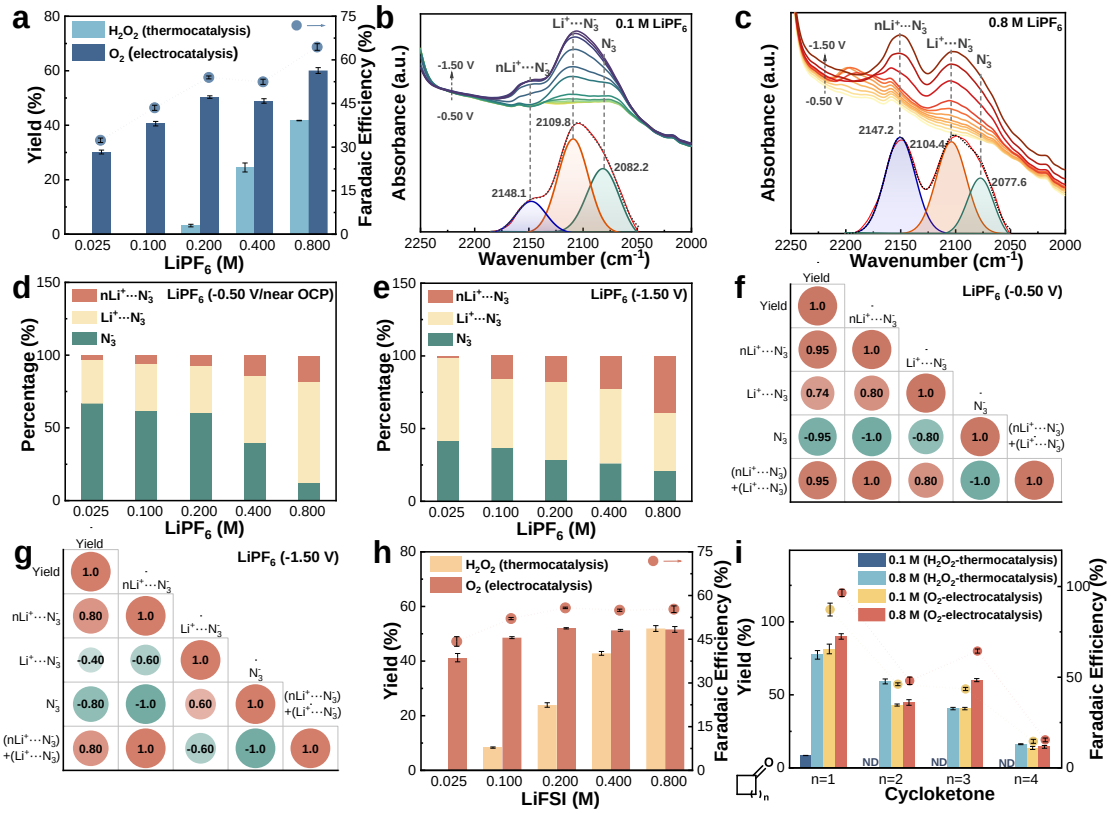

Figure 4. a) The yield and Faradaic efficiency of ε-CL in thermocatalytic/electrocatalytic scenarios with different $LiPF_6$ concentrations. b-c) The ATR-SEIRAS spectra of the system when polarized to different potentials in b) 0.1 M and c) 0.8 M $LiPF_6$ system with saturated N_3^-. d-e) The proportions of different forms of N_3^- and Li^+ coordinated-N_3^- in $LiPF_6$ systems with different concentrations d) near OCP and e) under -1.50 V vs. Fc/Fc^+. f-g) Kendall correlation coefficient between different forms of N_3^-/Li^+ coordinated-N_3^- and ε-CL yield f) near OCP and g) under -1.50 V vs. Fc/Fc^+. h) The yield and Faradaic efficiency of ε-CL in thermocatalytic/electrocatalytic scenarios with different LiFSI concentrations. i) Yield and Faradaic efficiency of different products for the oxygenation of different cycloketones under both thermocatalytic/electrocatalytic scenarios.